Research Article
Vol. 27, No. 12 | 10 Jun 2019 | OPTICS EXPRESS A909
Optics EXPRESS

Combining 1D and 2D waveguiding in an ultrathin GaAs NW/Si tandem solar cell

NASIM TAVAKOLI AND ESTHER ALARCON-LLADO*

Center for Nanophotonics, AMOLF, Science Park 104, 1098XG Amsterdam, The Netherlands
**e.alarconllado@amolf.nl*

Abstract: As an effective means to surpass the Shockley-Queisser efficiency limit, tandem solar cells have been successfully designed and used for years. However, there are still economical and design set-backs hampering the terrestrial implementation of tandem solar cells. Introducing high efficiency, thin Si-based tandem cells that are flexible in design (shape and curvature) will be the next major step towards integrating highly efficient solar cells into fashionable designs of today's buildings and technologies. In this work we present an optically coupled tandem cell that consists of a GaAs nanowire array on a 2μm-thick Si film as the top and bottom cells, respectively. By performing FDTD simulations, we show that coupling the incident light to guided modes of the 1D wires not only boosts the absorption in the wires, but also efficiently transfers the below bandgap photons to the Si bottom cell. Due to diffraction by the nanowire array the momentum of the transmitted light is matched to that of guided modes of the 2D Si thin film. Consequently, infrared light is up to four times more efficiently trapped in the Si bottom cell compared to when the film is not covered by the nanowires.

1. Introduction

Introducing thin, light-weight and high efficiency photovoltaics (PV) will make solar cells more suitable to be integrated in urban landscapes or even small gadgets and would largely contribute to solving the global warming threat that we are facing today. Designing such solar cells, however, is challenged by many set-backs. While stacking of solar cells with different characteristic bandgaps is the most common strategy to surpass the Shockley-Queisser efficiency limit, such tandem devices are typically heavy weight, rigid and costly. A fascinating strategy to potentially reduce both cost and rigidity is to combine thin film silicon (Si) PV (few micrometers in thickness) with semiconductor nanowire (NW) solar cells. The mechanical flexibility and resilience of micrometer thin cells introduces their adaptability to curved surfaces as well as the use of new potentially lighter encapsulation materials. The small footprint of the NWs breaks the lattice mismatch restriction so that any material combination is possible, including III-V/Si [1–8]. At the same time, the needle-like morphology of NWs results into a superior light absorption with respect to their thin film counterparts [9–16], which provides a path to save expensive and non-abundant elements such as indium or gallium. Experimental NW ensemble solar cells have shown similar extraordinary increase in conversion efficiencies as in hybrid perovskite-based PV. In only 8 years the conversion efficiency has increased from ~4% to almost 18% for InP and ~16% for GaAs [17–23].

Silicon is a highly desirable component in any tandem design thanks to the mature understanding of its optical and electronic properties as well as its widely available fabrication technologies. However, downscaling Si to few micrometers in thickness compromises the solar cell performance due to the poor Si absorption of infrared light and requires light management strategies. Diffraction gratings [24–26] and resonant nanostructures [27,28] have been proposed to improve light management in μm-thin silicon single junction cells. So far, no strategies have been proposed specifically for tandem designs.

#358091 https://doi.org/10.1364/OE.27.00A909
Journal © 2019 Received 18 Jan 2019; revised 16 Apr 2019; accepted 18 Apr 2019; published 22 May 2019

Although the combination of III-V semiconductor NWs with bulk Si as tandem cells has been studied both theoretically [29–34] and experimentally [35,36], the dramatic absorption loss in μm-thin Si films in this type of tandem cells and the possible solutions are yet to be studied.

In this work we demonstrate that optically coupled systems consisting of nanostructures and thin films in a tandem fashion can improve the overall solar cell performance beyond that of uncoupled counterparts. We show that light scattering in NW arrays can be smartly tuned to match the momentum of guided modes in the bottom cell. This way, the top cell provides two functionalities for the tandem device: 1) The GaAs NWs absorb the light so efficiently that filling only 10% of the volume is enough to have about the same fundamental PV efficiency limit as in a bulk GaAs cell, and 2) the grating effect of the NW array allows to couple the transmitted light to the guided modes of a 2 μm-thin Si slab, which quadruples light absorption in the Si cell.

2. Material and methods

In all calculations, the absorption spectra are obtained from FDTD simulations by using Lumerical software package. Computationally expensive FDTD simulations are done on the super computer LISA from SurfSara. The source in all the simulations is a broadband plane wave covering the wavelengths between 300 nm and 1200 nm. Complex refractive indices of the materials are taken by fitting polynomial functions to experimental data from Palik [37]. In the appendix 4.1, the calculated absorption with the fitted values and a broadband source is compared to that obtained when using the exact numbers in a frequency sweep.

The unit cell of all absorption simulations consist of one GaAs nanowire standing on a 2 μm-thick silicon film covered by a 200 nm thick Ag film underneath as a mirror and rear contact. Both substrates extend through the boundaries of the FDTD simulation area. The top and bottom boundaries are chosen to be Perfectly Matched Layers (PML) to guarantee total absorption of light and to prevent parasitic reflections from the top and bottom boundaries. For the simulations of NW arrays, the side boundaries are chosen to be periodic, resulting into a square array. For the simulations in which absorption and forward scattering cross sections are calculated for a single nanowire, a total field scattered field (TFSF) configuration is used and the side boundaries are chosen to be PMLs. TFSF is a predefined source in Lumerical which separates the scattered field from total field.

In order to calculate the conversion efficiency of our designed tandem cell, we use detailed balance principle in the radiative limit, namely only radiative recombination of photoexcited charge is taken into account as loss. This assumption will turn into ultimate thermodynamic efficiency limits, which is still far from real devices due to losses at contacts and the large non-radiative recombination rates, particularly relevant in NWs [38–41]. We have obtained the maximum conversion efficiency by calculating the electrical power as a function of bias voltage normalized by the incident power from the sun per unit surface area [$\eta = V \cdot J(V) / P_{solar}$]. The characteristic *J-V* curve of each cell is plotted by subtracting the dark current from the photogenerated current [$J(V) = J_{dark}(V) - J_{ph}$]. In the radiative limit, the bias dependent dark currents were calculated by:

$$J^{i}_{dark}(V) = \int_{200nm}^{4000nm} e \cdot em^{i}(\lambda) \cdot b^{i}_{e}(\lambda,\mu) d\lambda, \tag{1}$$

where e is the elementary charge, $\mu = eV$ is the electrochemical potential of the electron-hole pair, and i refers to either the GaAs-NW array or Si film. The electrochemical potential is assumed constant over the whole sub-cell structure. Due to reciprocity, the photon emission and absorption rates of the cell are equal, thus $em(\lambda) = abs(\lambda)$. The absorption spectra, $abs(\lambda)$, were obtained from the FDTD simulations, where normal incidence on the cell was considered. $b_e(\lambda,\mu)$ is the radiative emission rate per unit wavelength, described as

$$b_e(\lambda,\mu) = F_c \frac{2c}{\lambda^4}\left[\frac{1}{\left(e^{\frac{hc/\lambda-\mu}{k_B{*}T}}\right)-1}\right] \tag{2}$$

where c is the speed of light, k_B is the Boltzman's constant, T is the temperature in Kelvin and h is Planck's constant. F_c is a geometry factor that highlights the emission profile of the cell. It has been previously shown that the absorption spectrum in NW arrays is virtually constant up to angles ~75 degrees [42,43]. Despite experimental work on InP NW arrays with large pitch distances (2μm) have shown directional light emission mostly ruled by the individual NW geometry [44], theoretical work has shown that the directivities offered in NWs and NW arrays would only lead to about 20mV increase in the V_{OC} [45]. Thus, isotropic light emission towards the both upper and lower hemispheres was considered for simplicity in the NW array $(F_c = 4\pi)$ and only to the upper hemisphere in the thin film, $(F_c = 2\pi)$.

The photogenerated current (J_{ph}) of each cell is calculated by plugging the AM1.5G solar spectrum [$N_{ph}(\lambda)$] and the wavelength dependent absorption [$abs(\lambda)$] into the following equation:

$$J_{ph} = e \int_{300nm}^{\infty} N_{ph}(\lambda) abs(\lambda) d\lambda \tag{3}$$

Neglecting series or shunt resistance losses makes the short circuit current J_{SC} (i.e. current at V = 0) and J_{ph} to be the same. The maximum efficiency is given by $\frac{d}{dV}[J(V)V] = 0.$ The four terminal (4T) efficiency is calculated by adding the efficiencies of the top and bottom cells, without any restrictions on matching currents or voltages.

3. Results and discussion

In this paper, we present a combination of two waveguiding effects in NW-thin film tandem architectures. This concept combines the photonic properties of nanoscale semiconductors, the grating effect in ordered arrays with fabrication on low-cost silicon substrates. So far, coupling to the fundamental hybrid HE guided mode in vertically standing NWs has been used to maximize light absorption and PV efficiency in NW-based solar cells. By contrast, in this work we aim at taking additional advantage of the NW array configuration of the top cell as a grating coupler of sub-bandgap photons and funnel this light towards the thin bottom cell (See Fig. 1(a)). From now on, we will address the spectral range from 875 nm (bandgap of GaAs) to 1200 nm as NIR.

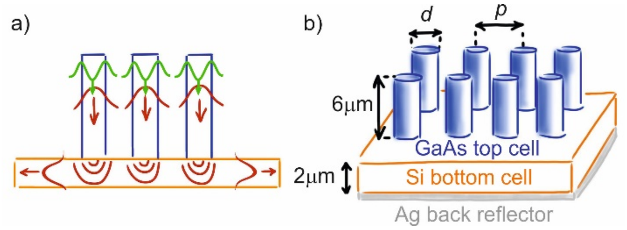

Fig. 1. a) Schematic representation of the combined 1D-2D waveguiding in the NW-thin film tandem solar cell. The NW geometry ensures the efficient coupling of a plane wave coupling to guided modes of the 1D waveguide NW. The interference between all scattered light generates an interference pattern at the bottom cell. This light will be coupled to 2D waveguide modes of the Si thin film. b) The geometry of our tandem cell, consisting of a square array of 6 μm long GaAs nanowires on a 2 μm Si slab. The 4T tandem cell is covered with 200 nm Ag at the back. Geometries can have different GaAs filling fractions by varying the diameter (d) and pitch distance (p).

As a proof of concept, we have considered a periodic 2D square array of GaAs NWs on top of a 2 µm-thick Si cell (see Fig. 1(b)), but the design principles apply to any combination of materials. The rear surface of the coupled system is covered with 200 nm silver as a back-reflector and possible back-contact. While the focus of this work is the optical properties proof of principle, we first only consider a GaAs NW array directly on top of a Si film for simplicity and to ensure an optimum optical coupling between the two cells. At the end of the manuscript, we address the potential losses that occur when considering a more realistic device structure.

A semiconductor NW that is illuminated parallel to its long axis acts as a 1D waveguide, the modes of which light can couple to very effectively when they are poorly confined [15,46–49]. The strength of light in-coupling is wavelength dependent and can be tuned by changing the diameter of the nanowire [11,46]. Fig. 2, shows the simulated absorption and forward scattering cross section of a single GaAs NW for different diameters. We have considered the light flux that is transmitted towards the lower half space of the simulation area as forward scattering. Both types of spectra show strong peaks in absorption/scattering that are ruled by the coupling to the NW guided modes, HE, the order of which is marked by a star (HE_{11}), triangle (HE_{12}), square (HE_{13}) and circle (HE_{14}). The position of the peaks shifts to longer wavelengths with diameter. In general, the best sunlight absorption is given by NWs with diameters, for which the peak in absorption related to the fundamental HE_{11} guided mode is close to the material's bandgap (diameter of 140 nm in GaAs). At larger diameters, efficient coupling to the HE_{11} mode occurs at wavelengths longer than that of the bandgap. Consequently the overall absorption decreases in favor of scattering. At even larger diameters, wavelengths close to the bangdap efficiently couples to higher order HE modes, resulting into both strong absorption and scattering (see for instance the spectra for the diameter of 500 nm).

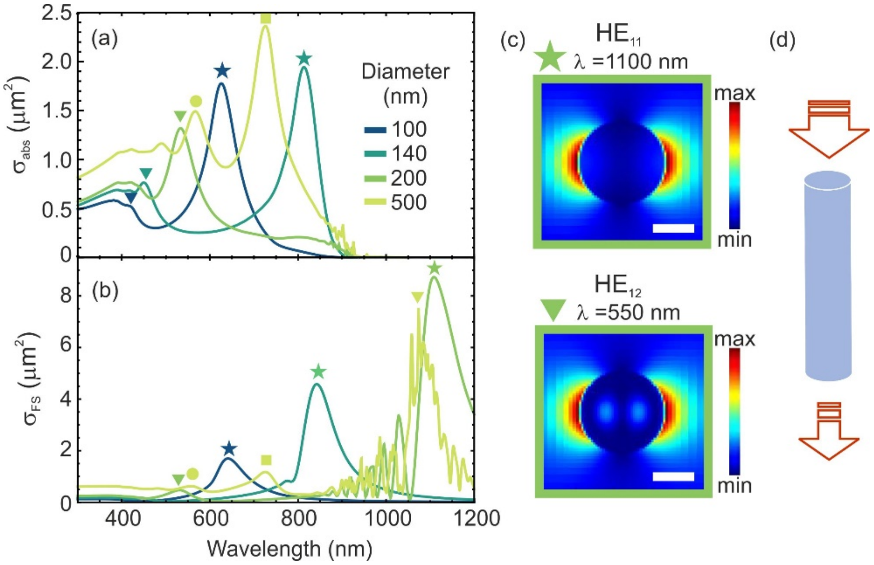

Fig. 2. Absorption (a) and forward scattering (b) cross section of a single GaAs nanowire of 6µm in length and various diameters. The peaks in absorption/forward scattering result from incoming light coupling to waveguiding modes of the NW, represented by different symbols according to the guided mode order. (c) Field intensity distribution in the axial cross-section of a NW of 200 nm in diameter at two different wavelengths, that highlight the coupling into the HE_{11} and HE_{12} guided modes. Scale bar is 100 nm. (d) Schematic representation of the simulation, where a plane wave is travelling along the main axis of the NW.

In the particular case of GaAs NWs with diameters of 200 and 500 nm a strong scattering peak related to the first and second order HE mode, respectively, lies in the 1000-1200nm spectral range. In this wavelength range, which is right at the Si bandgap edge (~1100nm), the light is efficiently scattered forward by the GaAs NWs to the Si film underneath, which can be very beneficial to the Si bottom cell.

In order to better quantify this effect in the tandem structure we have integrated the simulated absorption spectra of the NW array and Si film in the complete device design with the solar spectrum, and estimated the short circuit current for each sub-cell. Figure 3(a) shows the short circuit current (J_{sc}^{GaAs}) of the NW array as a function of NW diameter, calculated as described in the previous section. Different colors correspond to different NW pitch distances from 314 to 800 nm. In accordance to the previous section and previous works [20], J_{sc}^{GaAs} rapidly increases with the NW diameter followed by a decrease when the diameter increases beyond 150 nm. For pitch distances 500, 600, and in particular 800 nm, the absorption increases again at large diameters, as expected from the fact that a peak in absorption occurs near the bandgap due to light coupling into higher order guided modes. It is worth noting that, in all the arrays the ultimate absorption is less than that in a 6 μm-thick GaAs film and when the filling fraction is above ~0.2 (for instance, diameter of 160 nm for pitch distance 314 nm and diameter 400 nm for pitch distance 800 nm) the J_{sc}^{GaAs} decreases regardless of individual NW geometry. We attribute this loss in absorption due to increased reflectivity (see appendix 4.2 for more details) arising from the increased refractive index contrast at the Air/GaAs interface [50].

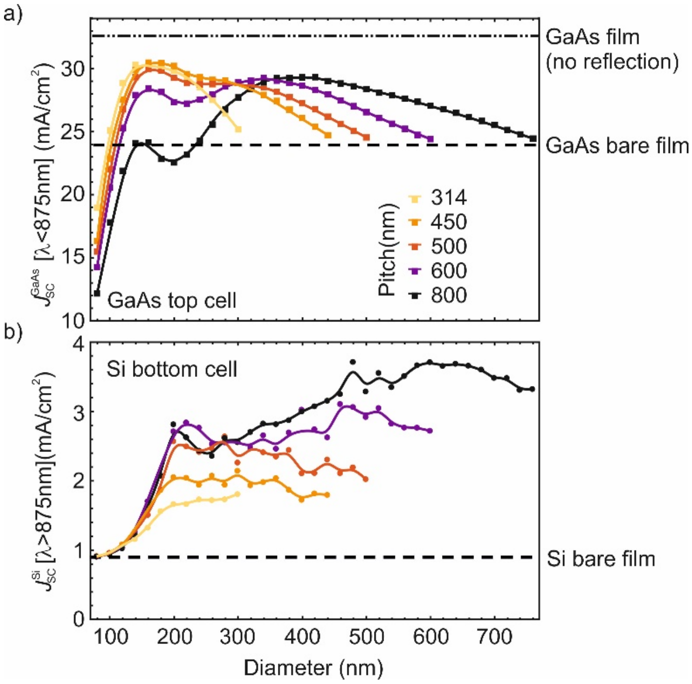

Fig. 3. a) Short circuit current (Jsc) of GaAs nanowire array (length: 6 μm) as a function of diameter, for pitch distances of 314, 450, 500, 600 and 800nm. b) Short circuit current in the Si film calculated for wavelengths longer than 875 nm, as a function of the GaAs NW array geometry. Arrays with pitch distances of 314, 450, 500, 600 and 800 nm are shown in different colors. The different lines correspond to the expected current densities of the cases as explained in the text.

Now we turn to the light absorption in the Si bottom cell. To highlight the optical effects of the top cell on the bottom one, Fig. 3(b) shows the J_{SC}^{Si} calculated from integrating the solar spectrum and the simulated Si absorption spectra only for energies below that of the bandgap of GaAs (i.e. $\lambda > 875$ nm). We plot the result as a function of GaAs NW diameter. Because in this wavelength range GaAs is transparent, changes in J_{SC}^{Si} ($\lambda > 875$ nm) for different NW array geometries must arise from the optical coupling of the two systems together. Different colors in the graph correspond to the different periodicities of the NW array.

In all the arrays studied here, $J_{SC}{}^{Si}$ (λ> 875 nm) is the same for the smallest NWs and it matches with the short circuit current for the same wavelength range of a free-standing Si film with a Ag back-reflector (0.9 mA/cm^2), which is represented by a horizontal dashed line in Fig. 3(b). This value is one order of magnitude smaller than what is attainable in bulk Si (9.8 mA/cm^2), if zero reflection is assumed. Interestingly, increasing the NW diameter rapidly increases the NIR-related current in Si, which in most cases it surpasses the expected current for the 2 μm-thick Si on Ag if (dash line in Fig. 3(b)). This is only true for diameters smaller than ~200nm, at which point the growth of $J_{SC}{}^{Si}$ (λ> 875 nm) with NW diameter is smaller. In the more sparse arrays, this change in the growth of the current at a diameter of 200 nm even results into a peak. A second peak is also discerned at diameters around 500-600 nm. The highest calculated $J_{SC}{}^{Si}$ (λ> 875 nm) in the 2 μm-thick Si is ~3.7 mA/cm^2, which represents almost 40% of the bulk reflection-less limit. The anti-reflection properties of the array cannot explain this trend, given that it is mostly ruled by the filling fraction instead of the NW diameter, and it detriments at filling fractions beyond 20%.

The fact that the NIR-related current is increased up to a factor 4 with respect to the bare Si film by incorporating a NW array top cell is a significant light trapping scheme that is obtained “for free” when using a nanostructured top cell. To confirm this link, we focus on the absorption spectrum in the Si film for the wavelength range between 875 nm and 1200 nm, Fig. 4(a). The dashed curve shows the absorption in a reference Si thin film in air (same thickness and with a Ag back-reflector), in which the Fabry-Pérot resonances are present. The solid curve shows the absorption of the same Si film with a top GaAs NW array of d = 200 nm and p = 800 nm. As compared to the bare film, additional sharp absorption peaks arise. We explain these sharp peaks as resonant coupling of light to the 2D waveguiding modes of the Si film, enabled by the coherent interference of scattered light by the NWs in the periodic array.

As in standard gratings, the scattered light from each NW coherently interferes and gives rise to a diffraction pattern. The in-plane momentum of the diffracted light ($k_{[mn]}^{diff} = ({}^{2\pi}\!/\!{}_{p})\sqrt{m^2+n^2}$, where p is the pitch distance and m and n are the diffraction orders in the two orthogonal in-plane directions) can be beyond the light cone in air enabling the diffracted light to couple into guided modes of the Si film. As a consequence, the effective optical mean path under such conditions is strongly enhanced and results into an increased short circuit current. Opposite to standard diffraction grating solutions in PV [51], in our design the brightness or intensity of the diffracted light by the NW array is strongly dependent on the NW diameter (see appendix 4.3). The effect proposed here is similar to light trapping strategies in thin film absorbers with the use of periodic arrays of metal or semiconductor resonators at either the front or rear-surfaces [52,53].

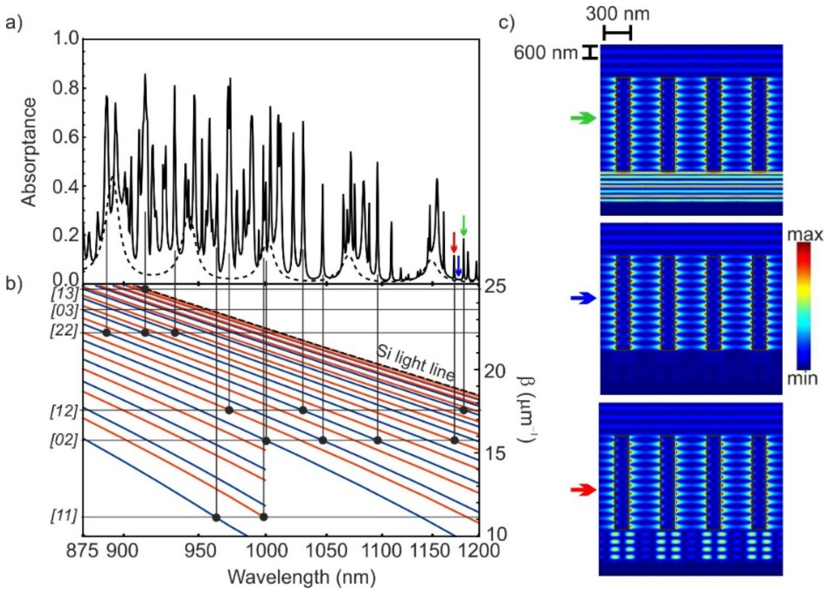

Fig. 4. a) Absorption spectra of the Si film without (dashed) and with (solid) the NW array on top in the NIR spectral range, for which GaAs is transparent. The NW array parameters are 800 nm pitch distance and 200 nm in diameter. b) Dispersion curves for TE and TM guided modes of a 2 μm Si slab, in red and blue respectively. The horizontal lines show the grating orders of a 2D periodic array with a 800 nm period. [mn] refer to the diffraction orders. Vertical lines are to highlight some intersections of the guided modes with the diffraction orders. c) Field distribution in a transverse cross-section of the full device for three different wavelengths, marked in the spectrum by arrows. The field profile at the peaks in absorption (green and red) match well with the excitation of the 7th order TE and 4th order TM guided modes in Si, respectively.

For completeness, we plot the dispersion relation of the TE and TM guided modes of 2 μm Si film in Fig. 4(b) (in blue and red, respectively). For the wavelength range of interest (875-1200 nm) the mode propagation constant (β) lies within the range of ~7 to 20 rad/μm. The modal calculations were done numerically by considering a 2 μm-thick Si film sandwiched between Ag and a dielectric of refractive index 1.45. The latter is a fair approximation to the refractive index of the NW-air ensemble in this wavelength range. The wavevectors for *[mn]* grating orders of a periodic NW array with pitch distance of 800 nm are displayed in horizontal solid black lines. As expected, the intersections between grating orders and guided modes coincide at the same wavelength where the absorption peaks occur. For clarity, not all intersections are shown. This highlights that the increase in Si absorption is not only affected by efficient forward scattering from each NWs, but is also strongly determined by whether or not the momentum of the transmitted light is matched to the 2D guided modes of the thin Si film. Further proof is given by the cross-sectional field energy distribution in the whole device structure for a wavelength where the momentum is matched (top and bottom plots in Fig. 4(c)). For comparison, we also include the field energy profile under non-matching conditions (middle plot). The increased photocurrent in Si due to diffraction-enabled coupling to guided modes also explains the strong dependence on pitch distance of the largest attainable J_{SC}^{Si} (λ> 875 nm) in Fig. 3(b). This means that the top GaAs NW array is not only active as a part of the solar cell, but also contributes to light trapping in the bottom Si cell.

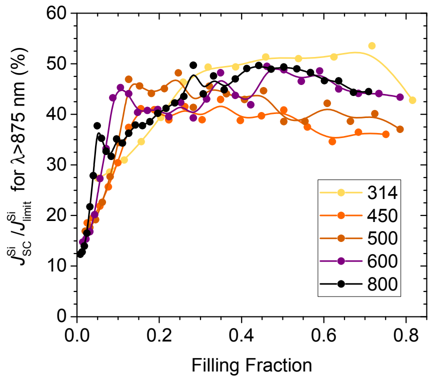

Fig. 5. Light trapping efficiency in the Si film as a function of the NW array filling fraction for arrays with different pitch distances. The efficiency is obtained by normalising the short circuit current in Si by that calculated considering the $4n^2\pi\ (p/\lambda)^2\alpha$ absorption limit.

To estimate the efficiency of the NW arrays to trap NIR photons in Si, we have calculated the ultimate J_{SC}^{Si} (λ> 875 nm) for a 2 µm Si film according to the Yablonovitch limit, which makes use of geometric optics and Lambertian texturing by considering a $4n^2$ enhancement of the absorption [54]. Within this framework, the ultimate current is 6 mA/cm^2, which results into a light trapping efficiency of 62% in the best case by using our design. While the Lambertian limit is commonly used in the community as a reference, its validity has been debated when considering nanostructures [55–58]. In particular, Yu et al. [59], found that a more accurate limit in a periodic grating whose periodicity (p) is smaller than the wavelength, considers the absorption to be enhanced by a factor $4n^2\pi(p/\lambda)^2$. This means that the ultimate light trapping of the NW array top cell is determined by the pitch distance. Figure 5 represents the light trapping efficiency in the Si film as a function of array filling fraction through the normalisation of the current by the periodicity-dependent limit. Interestingly, all the configurations have a similar trend in efficiency with ultimate values around 50%.

Last, we comment on the detailed balance conversion efficiency of our tandem design. Detail balance only considers radiative losses, which is in practice not attainable due to high surface or Auger recombinations. While the former is particularly true in GaAs NWs, Auger recombination limits the Silicon PV efficiency to ~94% of the detailed balance value in thin films [60]. Consequently, the efficiencies calculated here are thus slightly higher than what can be achieved in practice but it is a good figure of merit to compare the different tandem geometries.

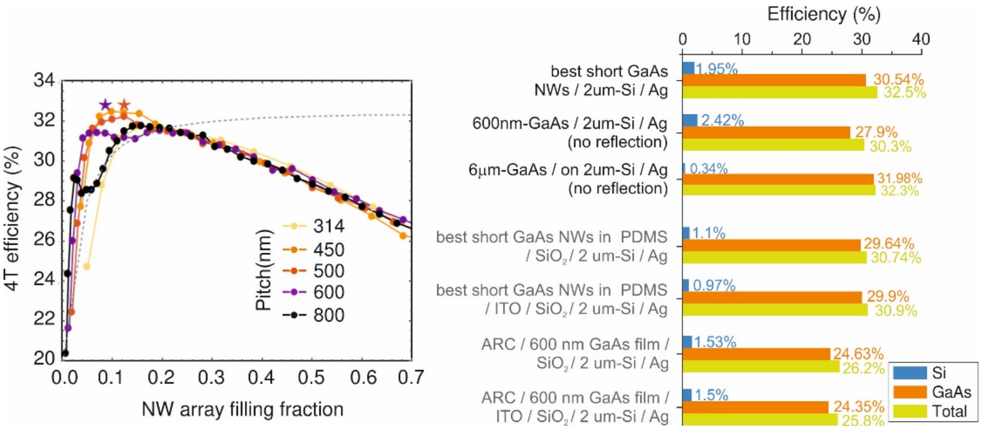

Fig. 6. Left: Detailed balance conversion efficiency of the 4T GaAs NW-Si film tandem cell as a function of GaAs array filling fraction. The NWs are 6 µm long and the Si is 2 µm thick. An Ag reflector is considered on the rear side. Different colors correspond to different pitch distances of the NW array. Stars show the total efficiency achieved by considering the NWs to be of 12 µm in length. The grey dashed line is the calculated 4T conversion efficiency of a GaAs equivalent film on 2 µm thick Si tandem, where the thickness of the GaAs film is such that it contains the same amount of material as in the array. Right: Summary of top, bottom and total cell efficiencies for our best performing designs along with the thin film and bulk equivalents. The geometry of the best short NWs is d = 160nm, p = 450nm. Realistic designs are labelled in grey. ARC refers to anti-reflective coating based on a 100 nm tick dielectric of n = 1.5.

The left plot in Fig. 6 is the four-terminal (4T) tandem conversion efficiency in the radiative limit as a function of GaAs NW array filling fraction, calculated as described in the methods section. The footprint of the GaAs array is tuned by changing both the diameter (d) and pitch distance (p) of the NW array. Different colours gather all data from same periodicities. We highlight two main observations in this plot in accordance to what has been described so far: 1) the maximum reachable efficiency strongly depends on the array geometry, and 2) after 20% of the surface being covered by GaAs the efficiency is independent of geometry and is limited by reflection. The grey dashed plot depicts the 4T efficiency of the film-equivalent GaAs-Si tandem, where the GaAs array is transformed into a film that contains the same amount of material. In this case, the efficiency is calculated by considering a double pass of the light and no reflection (see the appendix 4.4 for more details). In general, the highest PV efficiencies achieved in our calculations for the ultrathin tandem are when the top NW cell has a filling fraction around 5-15%. This is interesting when compared to the highest efficiency in the film-equivalent, where the more material the higher the PV efficiency. The best obtained efficiency based on our ultrathin NW/thin film design is ~32.5% for an array with p = 450nm and d = 160nm (i.e. only ~10% of the surface is covered by NWs). Despite this value being larger than the 30.3% obtained for its film-equivalent and just slightly higher than the 32.3% obtained in the case where the GaAs cell is a compact 6 µm-thick film on the 2 µm-Si/Ag bottom cell, it does not represent the best light trapping conditions in the bottom cell. According to Fig. 3(b), $d \geq 200$ nm and large p are best.

Arrays with larger pitch distances do not absorb all above bandgap photons. Thus, we have also calculated the total conversion efficiency by considering longer NWs (i.e., 12 µm) with d = 200 nm for a couple of pitch distance conditions. The resulting PV efficiency is represented by stars of corresponding colors in the left plot of Fig. 6. Now, the total conversion efficiency is increased to 32.8% and is virtually the same in both cases. We have summarized all the best efficiencies along with the contributions from each cell in a chart in

Fig. 6. While our design reaches efficiency values that are still well below the Shockley-Queisser limit for the bulk GaAs/Si tandem (38.7%), it over-performs the film-equivalent solution. The use of a hexagonal array configuration may improve the light absorption in the GaAs array, and thus the total efficiency. An even better solution might be the use of hyperuniform arrays with correlated disorder, where a continuous range of scattered momenta can be also tailored [61–63].

We have focused so far on the ultimate light absorption and detailed balance efficiency limit of the NW-Si coupled system, where the NW array is surrounded by air and a 4T configuration was assumed to avoid current matching conditions between top and bottom cells. In a realistic 4T device, an intermediate contact and an insulating layer must exist between the two cells and the NWs will most likely be embedded in a polymer support that planarizes the top surface. To illustrate this effects, we have also performed simulations by considering the NW array being supported by a PDMS matrix on a 100 nm-thick Indium Tin Oxide (ITO) as transparent contact and a 100 nm-thick SiO_2 layer as insulator. In the case of the thin film equivalent, we have also incorporated a standard anti-reflective coating (ARC) based on a 100 nm-thick dielectric of refractive index 1.5. In the realistic device design, the ultimate detailed balance efficiency is higher if the GaAs is shaped in the form of NWs (30.9 vs 25.8%), but overall lower than the idealistic case (32.5%). By comparing the efficiency numbers with those obtained in a realistic configuration without the ITO layer, one can see that most of the loss comes from NIR absorption at the ITO (see appendix 4.5 for more details). This is not unexpected and highlights the need for new transparent conductive materials as intermediate and top contacts that are photonically inactive.

In conclusion, we have introduced a tandem design for GaAs nanowires on µm-thick Si, in which the 1D waveguiding and scattering in GaAs NWs are combined with 2D waveguiding in Si film. While high order HE modes in the nanowires maximizes above GaAs bandgap photon absorption, lower order modes efficiently forward scatter NIR light to the Si bottom cell. Coherent interference between the nanowire scatterers creates a diffraction pattern, the momentum of which enables to increase the optical path in the Si film. While the interwire distance determines the number of resonances in the absorption spectrum of Si, the nanowire diameter determines the coupling strength and hence the redistribution of energy in the Si thin film. We proved the concept of waveguiding combination, and our design can lead to achieve 62% of the Yablonovitch absorption limit of the bottom Si cell. We believe that with better engineering of the k-space of the nanowire array, e.g. hyperuniform designs, the absorption in both top and bottom cell can be increased even further.

4. Appendix

4.1 Refractive index fitting sanity check

In order to check that the simulated absorption near the band gap edges by using a broadband source, and consequently fitted functions for the refractive indices, we performed two sets of simulations for one design case (NW array with pitch distance of 444 nm and a pillar diameter of 180 nm, on a 2-µm Si film on 200 nm Ag). In the first simulation we divided the source wavelength into three parts: from 300 nm to 830 nm, from 800 nm to 930 nm, and from 900 nm to 1200 nm, with a resolution of 0.5nm. By doing so we made sure to achieve a good fit to match experimental values of real and imaginary parts of refractive indices. We combined these three wavelength areas to cover the whole range. The absorption spectrum from this simulation is shown in black in Fig. 7. In the second simulation we performed a frequency sweep for our simulations with 1nm wavelength step, meaning that the source was changed from a broadband source to a single frequency source, effectively increasing the computational time by a factor of 190. The absorption spectrum can be seen in red. Due to the good agreement between the two spectra we chose the first approach for all the other simulations presented in this work.

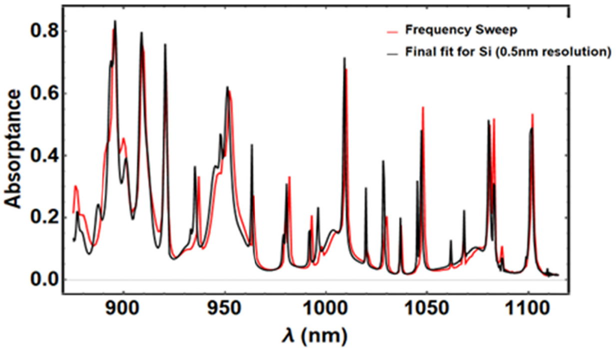

Fig. 7. Comparison of the NIR absorption spectra of the Si film when calculated using a fit to the Si optical parameters and broadband sources with respect to the experimental values and monochromatic light.

4.3 Reflectivity data

Figure 8 is the reflectance for the tandem structure (GaAs/Si/Ag) as a function of NW pitch distance and diameter. The reflectance has been calculated for the integrated spectrum of wavelengths < 875 nm, in order to avoid the long wavelength light that may not be absorbed by the Silicon film.

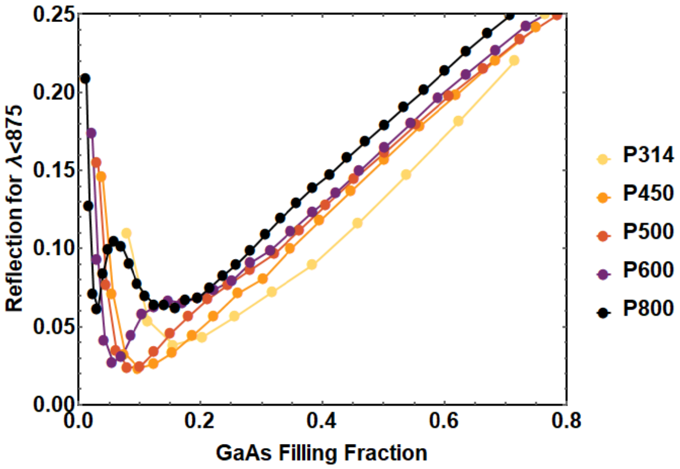

Fig. 8. Simulated reflectance in the visible spectral range for the Tandem device as a function of NW array filling fraction.

4.3 Si light absorption spectra as a function of GaAs NW diameter for p = 314nm

Figure 9 shows the absorption in Si thin film for 900<λ (nm)<1125 for a nanowire array with a pitch distance of 314 nm, and diameters of 80, 100, 140, 160, 180 and 200 nm. The sharp absorption peaks are present in all spectra at the exact same wavelength, but their intensity increases with NW diameter. This confirms that the peaks are rising from diffracted light entering Si slab from the NW array (namely, the wave vector or wavelength of the diffracted light only depends on the periodicity of the array). Second, the Fabry-Pérot (FP) peaks are apparent even in the case with largest diameters, arising from multiple reflections from the zero-order diffracted light. Note that the period of FP peaks in the cases of diameters 180 and 200nm nanowires seems to be smaller. This effect results from the fact that packed arrays on top of Si form the effective thickness of the dielectric slab to be larger which results in smaller periodicity of the FP peaks.

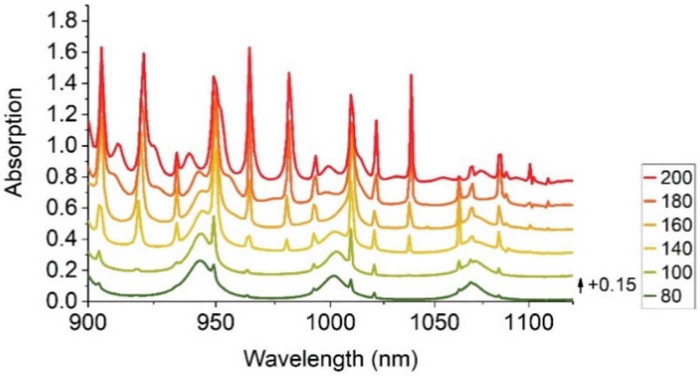

Fig. 9. Absorption in Si thin film for NIR range for a nanowire array with a pitch distance of 314 nm, and various diameters. Spectra are vertically shifted by 0.15 for clarity

4.4 Thin film-equivalent absorption calculations

As shown in Fig. 10, the absorption calculation for the thin film equivalent of the tandem design has been done using the Beer-Lambert law and neglecting reflection. In order to consider a realistic case, we assume the transmitted light from GaAs top cell to have a double pass in Si bottom cell, and then the remained transmitted light to pass through GaAs once more.

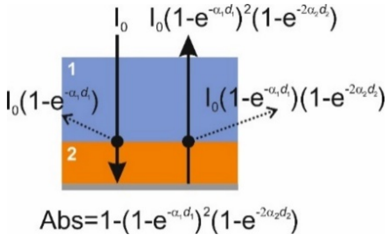

Fig. 10. Schematic representation of how is the double pass absorption being calculated for the thin film equivalent tandem designs

4.5 NIR absorption in ITO

The detrimental effects of the ITO/SiO_2 inter-layers in a realistic device configuration for the NIR absorption in Si mostly comes from the absorption in the ITO (Fig. 11).

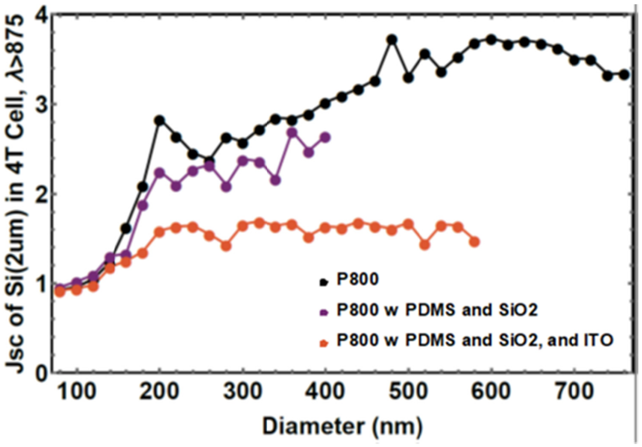

Fig. 11. Calculated NIR-related short circuit current in Si for: GaAs NWs/2um-Si/Ag (black), GaAs NWs in PDMS/SiO2/2um-Si/Ag (purple) and GaAs NWs in PDMS/ITO/SiO2/2um-Si/Ag (orange)

Funding

Netherlands Organisation for Scientific Research (NWO) (LMPV).

Acknowledgments

This work was carried out on the Dutch national e-infrastructure with the support of SURF Cooperative. Authors thank the support by the Light Management in Photovoltaics (LMPV) program, funded by the Foundation for Fundamental Research on Matter (FOM), which is part of The Netherlands Organization for Scientific Research (NWO). The authors thank T. P. N. Veeken, N. Schilder and F. Koenderik for fruitful discussions.

References

1. F. Glas, "Critical dimensions for the plastic relaxation of strained axial heterostructures in free-standing nanowires," Phys. Rev. B Condens. Matter Mater. Phys. **74**(12), 121302 (2006).
2. E. Russo-Averchi, M. Heiss, L. Michelet, P. Krogstrup, J. Nygard, C. Magen, J. R. Morante, E. Uccelli, J. Arbiol, A. Fontcuberta i Morral, and I. Morral, "Suppression of three dimensional twinning for a 100% yield of vertical GaAs nanowires on silicon," Nanoscale **4**(5), 1486–1490 (2012).
3. T. Mårtensson, C. P. T. Svensson, B. A. Wacaser, M. W. Larsson, W. Seifert, K. Deppert, A. Gustafsson, L. R. Wallenberg, and L. Samuelson, "Epitaxial III-V nanowires on silicon," Nano Lett. **4**(10), 1987–1990 (2004).
4. H. Kim, A. C. Farrell, P. Senanayake, W. J. Lee, and D. L. Huffaker, "Monolithically Integrated InGaAs Nanowires on 3D Structured Silicon-on-Insulator as a New Platform for Full Optical Links," Nano Lett. **16**(3), 1833–1839 (2016).
5. P. Krogstrup, R. Popovitz-Biro, E. Johnson, M. H. Madsen, J. Nygård, and H. Shtrikman, "Structural phase control in self-catalyzed growth of GaAs nanowires on silicon (111)," Nano Lett. **10**(11), 4475–4482 (2010).
6. M. Borg, H. Schmid, K. E. Moselund, G. Signorello, L. Gignac, J. Bruley, C. Breslin, P. Das Kanungo, P. Werner, and H. Riel, "Vertical III-V nanowire device integration on Si(100)," Nano Lett. **14**(4), 1914–1920 (2014).
7. L. C. Chuang, M. Moewe, C. Chase, N. P. Kobayashi, C. Chang-Hasnain, and S. Crankshaw, "Critical diameter for III-V nanowires grown on lattice-mismatched substrates," Appl. Phys. Lett. **90**(4), 043115 (2007).
8. C. Colombo, D. Spirkoska, M. Frimmer, G. Abstreiter, A. Fontcuberta i Morral, "Ga-assisted catalyst-free growth mechanism of GaAs nanowires by molecular beam epitaxy," Phys. Rev. B Condens. Matter Mater. Phys. **77**(15), 155326 (2008).
9. L. Hu and G. Chen, "Analysis of optical absorption in silicon nanowire arrays for photovoltaic applications," Nano Lett. **7**(11), 3249–3252 (2007).
10. N. Anttu and H. Q. Xu, "Efficient light management in vertical nanowire arrays for photovoltaics," Opt. Express **21**(S3 Suppl 3), A558–A575 (2013).
11. M. Heiss, E. Russo-Averchi, A. Dalmau-Mallorquí, G. Tütüncüoğlu, F. Matteini, D. Rüffer, S. Conesa-Boj, O. Demichel, E. Alarcon-Lladó, and A. Fontcuberta i Morral, "III-V nanowire arrays: growth and light interaction," Nanotechnology **25**(1), 014015 (2014).
12. P. Krogstrup, H. I. Jørgensen, M. Heiss, O. Demichel, J. V. Holm, M. Aagesen, J. Nygard, , A. Fontcuberta i

Morral, “Single-nanowire solar cells beyond the Shockley–Queisser limit,” Nat. Photonics **7**(4), 306–310 (2013).

13. K. T. Fountaine, C. G. Kendall, and H. A. Atwater, “Near-unity broadband absorption designs for semiconducting nanowire arrays via localized radial mode excitation,” Opt. Express **22**(S3), A930–A940 (2014).
14. G. Grzela, R. Paniagua-Domínguez, T. Barten, D. van Dam, J. A. Sánchez-Gil, and J. G. Rivas, “Nanowire Antenna Absorption Probed with Time-Reversed Fourier Microscopy,” Nano Lett. **14**(6), 3227–3234 (2014).
15. R. Frederiksen, G. Tutuncuoglu, F. Matteini, K. L. Martinez, A. Fontcuberta I Morral, and E. Alarcon-Llado, “Visual Understanding of Light Absorption and Waveguiding in Standing Nanowires with 3D Fluorescence Confocal Microscopy,” ACS Photonics **4**(9), 2235–2241 (2017).
16. N. Huang, C. Lin, and M. L. Povinelli, “Broadband absorption of semiconductor nanowire arrays for photovoltaic applications,” J. Opt. **14**(2), 024004 (2012).
17. J. Wallentin, N. Anttu, D. Asoli, M. Huffman, I. Aberg, M. H. Magnusson, G. Siefer, P. Fuss-Kailuweit, F. Dimroth, B. Witzigmann, H. Q. Xu, L. Samuelson, K. Deppert, and M. T. Borgström, “InP nanowire array solar cells achieving 13.8% efficiency by exceeding the ray optics limit,” Science **339**(6123), 1057–1060 (2013).
18. D. van Dam, N. J. J. van Hoof, Y. Cui, P. J. van Veldhoven, E. P. A. M. Bakkers, J. Gómez Rivas, and J. E. M. Haverkort, “High-Efficiency Nanowire Solar Cells with Omnidirectionally Enhanced Absorption Due to Self-Aligned Indium-Tin-Oxide Mie Scatterers,” ACS Nano **10**(12), 11414–11419 (2016).
19. I. Aberg, G. Vescovi, D. Asoli, U. Naseem, J. P. Gilboy, C. Sundvall, A. Dahlgren, K. E. Svensson, N. Anttu, M. T. Bjork, and L. Samuelson, “A GaAs nanowire array solar cell with 15.3% efficiency at 1 sun,” IEEE J. Photovoltaics **6**(1), 185–190 (2016).
20. M. Yao, N. Huang, S. Cong, C.-Y. Chi, M. A. Seyedi, Y.-T. Lin, Y. Cao, M. L. Povinelli, P. D. Dapkus, and C. Zhou, “GaAs Nanowire Array Solar Cells with Axial p-i-n Junctions,” Nano Lett. **14**(6), 3293–3303 (2014).
21. G. Mariani, P. S. Wong, A. M. Katzenmeyer, F. Léonard, J. Shapiro, and D. L. Huffaker, “Patterned radial GaAs nanopillar solar cells,” Nano Lett. **11**(6), 2490–2494 (2011).
22. T. Fukui, M. Yoshimura, E. Nakai, and K. Tomioka, “Position-controlled III-V compound semiconductor nanowire solar cells by selective-area metal-organic vapor phase epitaxy,” Ambio **41**(S2), 119–124 (2012).
23. G. Mariani, A. C. Scofield, C.-H. Hung, and D. L. Huffaker, “GaAs nanopillar-array solar cells employing in situ surface passivation,” Nat. Commun. **4**(1), 1497 (2013).
24. C. Trompoukis, O. El Daif, V. Depauw, I. Gordon, and J. Poortmans, “Photonic assisted light trapping integrated in ultrathin crystalline silicon solar cells by nanoimprint lithography,” Appl. Phys. Lett. **101**(10), 1–5 (2012).
25. A. Gaucher, A. Cattoni, C. Dupuis, W. Chen, R. Cariou, M. Foldyna, L. Lalouat, E. Drouard, C. Seassal, P. Roca I Cabarrocas, and S. Collin, “Ultrathin Epitaxial Silicon Solar Cells with Inverted Nanopyramid Arrays for Efficient Light Trapping,” Nano Lett. **16**(9), 5358–5364 (2016).
26. K. X. Wang, Z. Yu, V. Liu, Y. Cui, and S. Fan, “Absorption Enhancement in Ultrathin Crystalline Silicon Solar Cells with Antireflection and Light-Trapping Nanocone Gratings,” Nano Lett. **12**(3), 1616–1619 (2012).
27. I. Kim, D. S. Jeong, W. S. Lee, W. M. Kim, T.-S. Lee, D.-K. Lee, J.-H. Song, J.-K. Kim, and K.-S. Lee, “Silicon nanodisk array design for effective light trapping in ultrathin c-Si,” Opt. Express **22**(S6), A1431–A1439 (2014).
28. C. Lin, L. J. Martínez, and M. L. Povinelli, “Experimental broadband absorption enhancement in silicon nanohole structures with optimized complex unit cells,” Opt. Express **21**(S5), A872–A882 (2013).
29. L. Wen, X. Li, Z. Zhao, S. Bu, X. Zeng, J. H. Huang, and Y. Wang, “Theoretical consideration of III-V nanowire/Si triple-junction solar cells,” Nanotechnology **23**(50), 505202 (2012).
30. Y. Wang, Y. Zhang, D. Zhang, S. He, and X. Li, “Design High-Efficiency III-V Nanowire/Si Two-Junction Solar Cell,” Nanoscale Res. Lett. **10**(1), 968 (2015).
31. R. R. LaPierre, “Theoretical conversion efficiency of a two-junction III-V nanowire on Si solar cell,” J. Appl. Phys. **110**(1), 014310 (2011).
32. A. Benali, J. Michallon, P. Regreny, E. Drouard, N. Chauvin, D. Bucci, A. Fave, and A. Kaminski-cachopo, “Optical simulation of multijunction solar cells based on III-V nanowires on silicon,” Energy Procedia **60**, 109–115 (2014).
33. Y. Chen, O. Höhn, N. Tucher, M. E. Pistol, and N. Anttu, “Optical analysis of a III-V-nanowire-array-on-Si dual junction solar cell,” Opt. Express **25**(16), A665–A679 (2017).
34. N. Huang, C. Lin, M. L. Povinelli, N. Huang, C. Lin, and M. L. Povinelli, “Limiting efficiencies of tandem solar cells consisting of III-V nanowire arrays on silicon Limiting efficiencies of tandem solar cells consisting of III-V nanowire arrays on silicon,” J. Appl. Phys **112**(6), 064321 (2013).
35. M. Yao, S. Cong, S. Arab, N. Huang, M. L. Povinelli, S. B. Cronin, P. D. Dapkus, and C. Zhou, “Tandem Solar Cells Using GaAs Nanowires on Si: Design, Fabrication, and Observation of Voltage Addition,” Nano Lett. **15**(11), 7217–7224 (2015).
36. B. Wood, P. Kuyanov, M. Aagesen, and R. R. LaPierre, “GaAsP nanowire-on-Si tandem solar cell,” J. Photonics Energy **7**(04), 042502 (2017).
37. E. D. Palik, *Handbook of Optical Constants of Solids* (Academic Press, 1998).
38. N. Anttu, “Physics and design for 20% and 25% efficiency nanowire array solar cells,” Nanotechnology **30**(7), 074002 (2019).
39. S. A. Mann, S. Z. Oener, A. Cavalli, J. E. M. Haverkort, E. P. A. M. Bakkers, and E. C. Garnett, “Quantifying losses and thermodynamic limits in nanophotonic solar cells,” Nat. Nanotechnol. **11**(12), 1071–1075 (2016).
40. N. Tajik, Z. Peng, P. Kuyanov, and R. R. LaPierre, “Sulfur passivation and contact methods for GaAs nanowire solar cells,” Nanotechnology **22**(22), 225402 (2011).
41. C. E. Chia and R. R. LaPierre, “Electrostatic model of radial pn junction nanowires,” J. Appl. Phys. **114**(7),

074317 (2013).
42. N. Anttu and H. Q. Xu, “Coupling of Light into Nanowire Arrays and sub Sequent Absorption,” J. Nanosci. Nanotechnol. **10**(11), 7183–7187 (2010).
43. N. Anttu, “Shockley-queisser detailed balance efficiency limit for nanowire solar cells,” ACS Photonics **2**(3), 446–453 (2015).
44. D. van Dam, D. R. Abujetas, R. Paniagua-Domínguez, J. A. Sánchez-Gil, E. P. A. M. Bakkers, J. E. M. Haverkort, and J. Gómez Rivas, “Directional and Polarized Emission from Nanowire Arrays,” Nano Lett. **15**(7), 4557–4563 (2015).
45. S. A. Mann, R. R. Grote, R. M. Osgood, Jr., A. Alù, and E. C. Garnett, “Opportunities and Limitations for Nanophotonic Structures To Exceed the Shockley-Queisser Limit,” ACS Nano **10**(9), 8620–8631 (2016).
46. S. Mokkapati, D. Saxena, H. H. Tan, and C. Jagadish, “Optical design of nanowire absorbers for wavelength selective photodetectors,” Sci. Rep. **5**(1), 15339 (2015).
47. V. Dagytė and N. Anttu, “Modal analysis of resonant and non-resonant optical response in semiconductor nanowire arrays,” Nanotechnology **30**(2), 025710 (2019).
48. N. Anttu, “Absorption of light in a single vertical nanowire and a nanowire array,” Nanotechnology **30**(10), 104004 (2019).
49. K. T. Fountaine, W. Whitney, and H. A. Atwater, “Resonant absorption in semiconductor nanowires and nanowire arrays: Relating leaky waveguide modes to Bloch photonic crystal modes,” J. Appl. Phys. **116**(15), 153106 (2014).
50. C. Lin, N. Huang, and M. L. Povinelli, “Effect of aperiodicity on the broadband reflection of silicon nanorod structures for photovoltaics,” Opt. Express **20**(1), A125–A132 (2012).
51. A. Mellor, I. Tobias, A. Martí, M. J. Mendes, and A. Luque, “Upper limits to absorption enhancement in thick solar cells using diffraction gratings,” Prog. Photovolt. Res. Appl. **19**(6), 676–687 (2011).
52. G. Yin, M. W. Knight, M. Van Lare, M. Sola-Garcia, A. Polman, and M. Schmid, “Optoelectronic Enhancement of Ultrathin CuIn 1 – x Ga x Se 2 Solar Cells by Nanophotonic Contacts,” Adv. Opt. Mater. **5**(5), 1600637 (2017).
53. S. Mokkapati, F. J. Beck, A. Polman, and K. R. Catchpole, “Designing periodic arrays of metal nanoparticles for light-trapping applications in solar cells,” Appl. Phys. Lett. **95**(5), 93–96 (2009).
54. E. Yablonovitch, “Statistical ray optics,” J. Opt. Soc. Am. **72**(7), 899–907 (1982).
55. T. Markvart, “Beyond the Yablonovitch limit: Trapping light by frequency shift,” Appl. Phys. Lett. **98**(7), 7–9 (2011).
56. A. Oskooi, Y. Tanaka, and S. Noda, “Tandem photonic-crystal thin films surpassing Lambertian light-trapping limit over broad bandwidth and angular range,” Appl. Phys. Lett. **104**(9), 091121 (2014).
57. J. Bhattacharya, N. Chakravarty, S. Pattnaik, W. Dennis Slafer, R. Biswas, and V. L. Dalal, “A photonic-plasmonic structure for enhancing light absorption in thin film solar cells,” Appl. Phys. Lett. **99**(13), 131114 (2011).
58. S. E. Han and G. Chen, “Toward the Lambertian limit of light trapping in thin nanostructured silicon solar cells,” Nano Lett. **10**(11), 4692–4696 (2010).
59. Z. Yu, A. Raman, and S. Fan, “Fundamental limit of light trapping in grating structures,” Opt. Express **18**(S3 Suppl 3), A366–A380 (2010).
60. M. J. Kerr, A. Cuevas, and P. Campbell, “Limiting Efficiency of Crystalline Silicon Solar Cells Due to Coulomb-Enhanced Auger Recombination,” Prog. Photovolt. Res. Appl. **11**(2), 97–104 (2003).
61. E. R. Martins, J. Li, Y. Liu, V. Depauw, Z. Chen, J. Zhou, and T. F. Krauss, “Deterministic quasi-random nanostructures for photon control,” Nat. Commun. **4**(1), 2665 (2013).
62. V. E. Ferry, M. A. Verschuuren, M. C. Lare, R. E. I. Schropp, H. A. Atwater, and A. Polman, “Optimized spatial correlations for broadband light trapping nanopatterns in high efficiency ultrathin film a-Si:H solar cells,” Nano Lett. **11**(10), 4239–4245 (2011).
63. C. Carlson and S. Hughes, “Disordered nanophotonic surfaces for enhanced light collection in semiconductor solar cells,” J. Opt. Soc. Am. B **35**(5), 1093–1104 (2018).